An electroceutical approach enhances myelination via upregulation of lipid biosynthesis in the dorsal root ganglion

IOP Publishing Biofabrication 14 (2022) 015017 https://doi.org/10.1088/1758-5090/ac457c

Biofabrication

PAPER

An electroceutical approach enhances myelination via upregulation of lipid biosynthesis in the dorsal root ganglion

Aseer Intisar[1], Woon-Hae Kim[2], Hyun Young Shin[2,6], Min Young Kim[1], Yu Seon Kim[3], Heejin Lim[1], Hyun Gyu Kang[1], Yun Jeoung Mo[3], Mohamed Aly Saad Aly[1], Yun-Il Lee[3] and Minseok S Kim[1,4,5,*]

[1] Department of New Biology, DGIST, Daegu 42988, Republic of Korea
[2] CTCELLS Corp., Daegu 42988, Republic of Korea
[3] Well Aging Research Center, DGIST, Daegu 42988, Republic of Korea
[4] Translational Responsive Medicine Center (TRMC), DGIST, Daegu 42988, Republic of Korea
[5] New Biology Research Center (NBRC), DGIST, Daegu 42988, Republic of Korea
[6] SBCure Corp., Daegu 43017, Republic of Korea
[*] Author to whom any correspondence should be addressed.

E-mail: kms@dgist.ac.kr

Keywords: electroceuticals, myelination, lipid biosynthesis, secondary ion mass spectrometry, myelin lipids, dorsal root ganglion

Supplementary material for this article is available online

OPEN ACCESS

RECEIVED
3 October 2021

REVISED
15 December 2021

ACCEPTED FOR PUBLICATION
21 December 2021

PUBLISHED
6 January 2022

Abstract

As the myelin sheath is crucial for neuronal saltatory conduction, loss of myelin in the peripheral nervous system (PNS) leads to demyelinating neuropathies causing muscular atrophy, numbness, foot deformities and paralysis. Unfortunately, few interventions are available for such neuropathies, because previous pharmaceuticals have shown severe side effects and failed in clinical trials. Therefore, exploring new strategies to enhance PNS myelination is critical to provide solution for such intractable diseases. This study aimed to investigate the effectiveness of electrical stimulation (ES) to enhance myelination in the mouse dorsal root ganglion (DRG)—an *ex vivo* model of the PNS. Mouse embryonic DRGs were extracted at E13 and seeded onto Matrigel-coated surfaces. After sufficient growth and differentiation, screening was carried out by applying ES in the 1–100 Hz range at the beginning of the myelination process. DRG myelination was evaluated via immunostaining at the intermediate (19 days *in vitro* (DIV)) and mature (30 DIV) stages. Further biochemical analyses were carried out by utilizing ribonucleic acid sequencing, quantitative polymerase chain reaction and biochemical assays at both intermediate and mature myelination stages. Imaging of DRG myelin lipids was carried out via time-of-flight secondary ion mass spectrometry (ToF-SIMS). With screening ES conditions, optimal condition was identified at 20 Hz, which enhanced the percentage of myelinated neurons and average myelin length not only at intermediate (129% and 61%) but also at mature (72% and 17%) myelination stages. Further biochemical analyses elucidated that ES promoted lipid biosynthesis in the DRG. ToF-SIMS imaging showed higher abundance of the structural lipids, cholesterol and sphingomyelin, in the myelin membrane. Therefore, promotion of lipid biosynthesis and higher abundance of myelin lipids led to ES-mediated myelination enhancement. Given that myelin lipid deficiency is culpable for most demyelinating PNS neuropathies, the results might pave a new way to treat such diseases via electroceuticals.

1. Introduction

The myelin sheath plays several important roles in the proper function of neurons: it maintains saltatory conduction during neuronal transmission, supports neurons by providing trophic factors and assists in regeneration [1–3]. Therefore, the loss of myelin in the peripheral nervous system (PNS) can lead to demyelinating neuropathies, causing muscular atrophy, foot deformities, paresthesia, numbness and paralysis [4]. For example, Charcot-Marie-Tooth (CMT) disease is one of the most commonly inherited neuropathies worldwide and constitutes majority of all demyelinating PNS neuropathies [5].

Since a common abnormality in several peripheral demyelinating neuropathies—including CMT—is an impeded *de novo* lipid biosynthesis pathway in the PNS [6], treatment strategies involving exogenous lipid supplementation have been studied with phosphatidylcholine and high-fat diet [7, 8]. However, elevated phosphatidylcholine levels aggravate the manifestation of cardiovascular diseases and a high-fat diet leads to obesity as well as insulin resistance—which have long-lasting ramifications [9–12]. Meanwhile, previous studies using ascorbic acid showed improvements in myelination in the preclinical stage but failed to show any significant benefit in clinical trials [13, 14]. Unfortunately, due to the potential side effects as well as the lack of success of the previous approaches, establishing effective intervention for demyelinating diseases has remained as an unresolved challenge [15]. Therefore, it is critical to explore a new strategy that can enhance myelination with minimal side effects in the PNS.

Given that the functionality of the nervous system depends on excitatory signals, electrical stimulation (ES) has a potential to modulate the function of neuronal cells. It has already been demonstrated that ES can promote axonal regeneration after injury [16, 17], release of beneficial trophic factors from Schwann cells (SCs) [18, 19], neurite outgrowth, and amelioration of pain in the PNS [20, 21]. However, it has rarely been explored for the phenotypic enhancement of PNS myelination, not to mention for the mechanism study. Here, we introduce an electroceutical approach that can enhance the myelination in the PNS. Furthermore, we investigate the major pathway inducing the myelination for mechanistic insight.

In this study, we utilize the mouse embryonic dorsal root ganglion (DRG), which faithfully preserves the native cell population, cell–cell interactions, extracellular matrix and biochemical cues. Hence, it is considered a representative *ex vivo* model in PNS myelination study [22]. Unfortunately, the previous ES platforms utilized for DRG stimulation have several key limitations regarding (a) uniformity of the electric field generated, (b) simultaneous stimulation of multiple DRG samples, (c) maintenance of aseptic condition during the stimulation session, and (d) long-term culture of the DRG after stimulation has been provided [20, 23]. Therefore, to overcome the aforementioned limitations, we develop a novel ES platform that can simultaneously provide uniform ES to multiple DRG samples, and is a closed system to prevent contamination. Furthermore, the DRGs can be removed from the platform after stimulation and subsequently maintained in long-term culture for further analyses.

The optimal ES condition to improve myelination is identified by a screening step during which ES is applied in the frequency range of 1–100 Hz and the efficacy is determined by changes of Krox20 expression. The result reveals that 20 Hz is the optimal ES frequency at which Krox20 expression is significantly enhanced. Next, with the optimal ES condition, the myelination is inspected at both the intermediate and mature stages of the myelination process. Upon the application of ES at 20 Hz, the percentage of myelinated neurons and the average myelin length in the DRG show a significant enhancement at both stages. To evaluate this change at a biochemical level, ribonucleic acid (RNA) sequencing is carried out at both the aforementioned stages. Results show that the lipid biosynthesis pathway—one of the major pathways commonly downregulated in demyelinating peripheral neuropathies—is consistently upregulated. Furthermore, consistently upregulated genes involved in PNS myelination pathway are also observed. For further validation, quantitative polymerase chain reaction (qPCR) and biochemical assays are conducted, which corroborate the upregulation in *de novo* lipid biosynthesis. Finally, lipid imaging via time-of-flight secondary ion mass spectrometry (ToF-SIMS) is performed to verify whether the upregulation in lipid biosynthesis results in increased abundance of myelin membrane lipids. The ToF-SIMS images of DRGs show the enhancement of cholesterol and sphingomyelin—two important structural lipids of the myelin membrane—in myelin-like segments. Based on the results, this study shows the enhancement of DRG myelination upon ES, resulting from lipid biosynthesis which leads to better abundance of structural lipids in the myelin membrane (figure 1).

2. Experimental section

2.1. Dorsal root ganglion (DRG) culture

DRGs were extracted from thoracic region of 13 d old mouse embryos. Each DRG was positioned gently at the center of a coverslip coated with a thin layer of Matrigel (Corning; product number: 356231) and placed in 24 well plates (Corning; product number: 3526). DRGs were cultured in growth medium for 8 d, followed by myelination medium for the rest of the culture period. The compositions of growth and myelination media are given in table S1 (available online at stacks.iop.org/BF/14/015017/mmedia).

2.2. Electrical stimulation (ES) device

The 3D modeling for the device was carried out using SolidWorks®, and it was fabricated via computerized numerical control machine using polyetheretherketone (PEEK). PEEK enables autoclaving for sterilization and offers excellent dimensional stability and oxidation resistance. These properties make it ideal to be used in ES devices for biological applications. The device had an inner diameter of 100 mm and depth of 14 mm. It consisted of six wells, each with a diameter of 15 mm and surrounded by three miniature pillars to securely hold the coverslip in position. The electrodes were made from stainless steel, and then

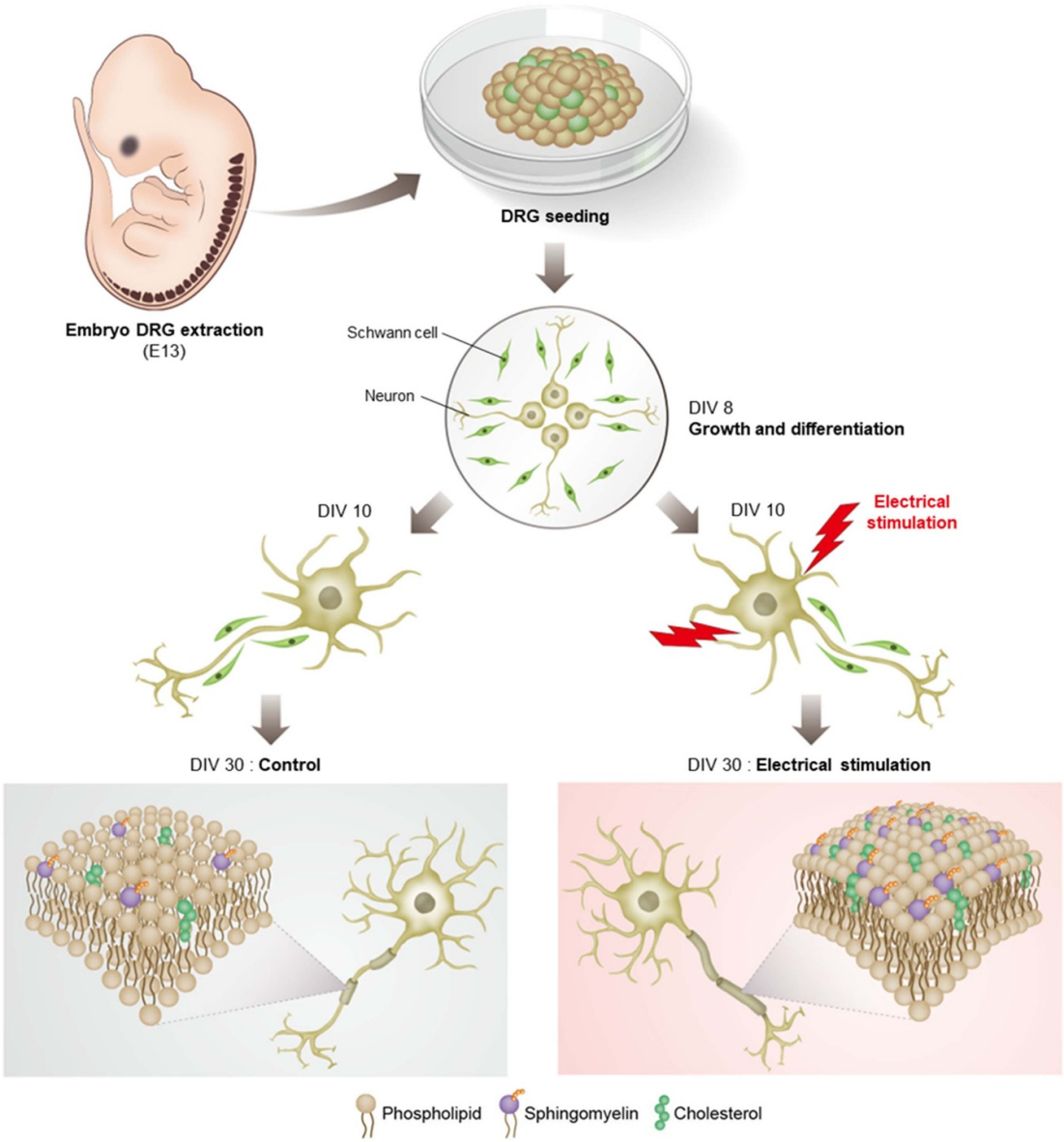

Figure 1. Schematic outlining the approach and outcome of this work. Mouse embryonic DRG was extracted and seeded on a Matrigel-coated surface. The neurons and SCs in the DRG were allowed to grow and differentiate before changing the medium to myelination medium (DIV 8). ES was applied at the beginning of the myelination process (DIV 10). Further analyses showed that ES led to an enhancement in myelination of DRG neurons, resulting from higher abundance of structural lipids of myelin, such as cholesterol and sphingomyelin.

electroplated with a 2 μm thick nickel undercoat (for adhesion with gold layer) followed by a 0.5 μm thick gold layer. Each electrode had a length of 70 mm, height of 6 mm and width of 1 mm. During assembly, the electrodes were positioned 30 mm apart and parallel to each other. After assembly, the electrodes were held in place using slits in the upper and lower chambers (figure 2(A)). COMSOL Multiphysics® was used (with electro-conductive properties of the medium based on Dulbecco's Modified Eagle Medium) to simulate the uniformity of the electrical field generated across each well (figure 2(B)).

2.3. Electrical stimulation (ES) of DRGs

ES was provided to the embryo DRGs at 10 days *in vitro* (DIV). The coverslips containing the DRGs were positioned within the wells of the ES device and then 15 ml myelination medium was added to the device. A biphasic square wave was generated at 50 mV mm^{-1} and the stimulation was provided for 1 h. ES was provided at 1, 20 and 100 Hz during the screening and only 20 Hz during the rest of the steps. After the ES application, the DRGs were placed back into 24 well plates.

2.4. Immunocytochemistry

Cells were fixed with 4% paraformaldehyde treatment for 15 min at room temperature (RT). The fixed cells were then blocked by treatment with blocking buffer (1 × phosphate-buffered saline (PBS), 0.3% Triton X-100 and 5% Normal Donkey Serum) for 1 h. After blocking, primary antibodies were added, diluted in

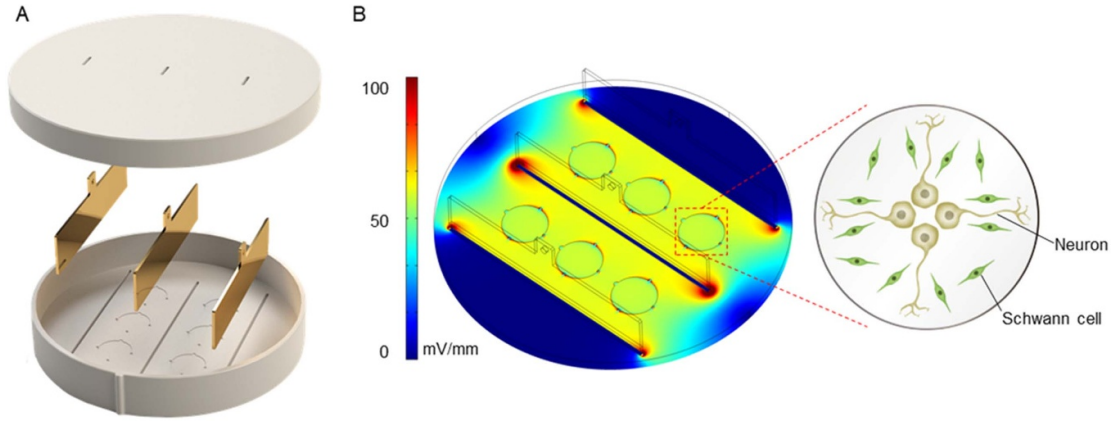

Figure 2. The device used for ES. (A) The configuration of the ES device used. The lower chamber can securely hold six coverslips during stimulation. The upper chamber holds the three electrodes parallel to each other after full assembly. (B) COMSOL Multiphysics simulation showing the uniformity of the electric fields across all six wells while generating 50 mV mm^{-1}. The coverslip containing the DRG explant is held securely within the well during stimulation.

antibody dilution buffer (ADB; 1 × PBS, 0.3% Triton X-100 and 1% Normal Donkey Serum). This was left at 4 °C in the refrigerator overnight. Then, secondary antibodies were added, diluted in ADB, and kept at RT in a dark environment for 1 h.

Primary antibodies: rabbit monoclonal anti-myelin basic protein (MBP) (Abcam; catalogue number: ab40390; used at 1:200 dilution) and mouse monoclonal anti-Tuj-1 (Abcam; catalogue number: ab78078; used at a 1:1000 dilution). Secondary antibodies: donkey anti-rabbit Alexa fluor® 488 (Jackson ImmunoResearch; catalogue number: 711-545-152; used at 1:200 dilution), donkey anti-mouse Alexa fluor® 594 (Jackson ImmunoResearch; catalogue number: 715-585-151; used at 1:200 dilution). For the average myelin length, the lengths of individual myelin segments were measured from 4X images using the NeuronJ plugin (for facilitating tracing and analysis of neuronal images) of ImageJ. Measurement for percentage of myelinated neurons was obtained via co-localization of MBP with Tuj-1 from 4X images using Colocalization Finder plugin of ImageJ. For these measurements, there were three biologically distinct replicates from each condition and three technical replicates from each biological replicate.

2.5. RNA sequencing

RNA was extracted from the whole DRGs using TRIzol Reagent (Thermo Fisher; catalogue number: 15596018), according to the manufacturer's instructions. For each condition, RNA was harvested from three DRG explants pooled together. RNA quality was assessed by Agilent 2100 Bioanalyzer using the RNA 6000 Nano Kit (Agilent Technologies, CA, USA). RNA quantification was performed using ND-2000 Spectrophotometer (Thermo Fisher, MA, USA). The construction of RNA library was performed using QuantSeq 3′ mRNA-Seq Library Prep Kit (Lexogen, Austria), according to the manufacturer's instructions. High-throughput sequencing was performed as single-end 75 sequencing using NextSeq 500 (Illumina, CA, USA). Alignment was performed using Bowtie2 [24]. Bowtie2 indices were either generated from genome assembly sequence or the representative transcript sequences for aligning to the genome and transcriptome, using the mm10 (Mus musculus) genome assembly. The alignment file was used for assembling transcripts, estimating their abundances and detecting differential expression of genes. Differentially expressed genes were determined based on counts from unique and multiple alignments using coverage in BEDTools [25]. The RC (read count) data were processed based on quantile normalization method using edgeR package from Bioconductor within R [26]. Gene classification was based on searches done by Database for Annotation, Visualization, and Integrated Discovery (DAVID) (https://david.ncifcrf.gov/) and Medline databases (www.ncbi.nlm.nih.gov/). Differential analysis and graphic visualization were performed using ExDEGA (Ebiogen, Republic of Korea). Protein association networks were created using the STRING plugin of Cytoscape (version 3.7.2). The RNA sequencing data in this study have been deposited to the Gene Expression Omnibus database of the National Center for Biotechnology Information under the accession number GSE190745.

2.6. Quantitative polymerase chain reaction (qPCR)

For messenger RNA (mRNA) extraction, Rneasy Mini Kit (Qiagen; catalogue number: 74106) was used. All separation and purification steps carried out were done according to the protocol provided with the kit. This was followed by complementary deoxyribonucleic acid (cDNA) synthesis, using AccuPower® RT

Premix (Bioneer; catalogue number: K-2041-B). The temperature cycling was done using Biometra Tone (Analytik Jena), with the recommended temperature and duration for the AccuPower® RT Premix. Real-time PCR was carried out on three biologically distinct samples from each group—control and ES DRGs—at each time point. Three technical replicates were prepared for each sample and average C_T value was taken for further comparison. Applied Biosystems StepOnePlus™ was used for thermal cycling and C_T measurements, and the software StepOne v2.3 available from Applied Biosystems was used to directly calculate the fold change in the ES DRGs compared to the control. The mixtures and temperature cycles used were according to the guideline provided with the instrument. The list of sequences for primers used is provided in table S2.

2.7. Citrate and carnitine assay

Citrate assay was performed using Citrate Assay Kit (Abcam; catalogue number: ab83396) and carnitine assay was performed using L-Carnitine Assay Kit (Abcam; catalogue number: ab83392). All further steps were carried out according to the manual provided with the respective kit. The assays were carried out on three biological replicates for each group and twice for each biological replicate, as recommended in the manual. Data shown in the graphs of the respective assays show measurements from all repetitions. The absorbance was measured by VersaMax Microplate Reader (Molecular Devices) at a wavelength of 570 nm.

2.8. Time-of-flight secondary ion mass spectrometry (ToF-SIMS)

Cells were fixed by treating with formalin solution (10%; Sigma Aldrich) for 10 min followed by glutaraldehyde solution (20%; Electron Microscopy Sciences) for 15 min, both at RT. The DRGs were post-fixed in osmium tetroxide solution (0.4%; Sigma Aldrich) for 15 min at RT and then air-dried. Prior to ToF-SIMS imaging, the cells were treated by air-plasma (CUTE, Femto Science Inc., Republic of Korea) at 1.1–1.3 Torr, 50 kHz, 100 W, and 70 sccm of air for 5 min. Analysis was conducted on a ToF-SIMS 5-100 instrument (ION-TOF, Münster, Germany) using a pulsed 30 keV Bi_3^+ primary ion beam in delayed extraction mode. ToF-SIMS images were obtained from fixed DRG on a cover glass over an area of 300 × 300 μm^2 with 256 × 256 pixels. Internal mass calibration for ToF-SIMS spectra was performed using the peaks of CH_3^+, Na^+, $C_2H_3^+$, $C_3H_5^+$and $C_4H_7^+$ for positive ion mode, and C^-, C_2^-, C_3^- and C_4^- for negative ion mode before further analysis. Low-energy electrons were supplied onto the surface of the sample using an electron flood gun for charge compensation during analysis.

2.9. Statistical analyses

Values are expressed as mean ± s.d. Statistical significance was calculated with GraphPad Prism software (version 8.0). One-way analysis of variance (ANOVA) followed by Tukey's comparison test was used to compare the groups ($^*P < 0.05$, $^{**}P < 0.005$ and $^{***}P < 0.001$).

3. Results

3.1. ES enhances DRG myelination

The DRGs were extracted from mouse embryos at E13, seeded onto Matrigel-coated coverslips, and supplemented with growth medium. After sufficient growth and differentiation of neurons and SCs in the DRG, myelination was induced using the myelination medium (DIV 8). After allowing the DRG to sufficiently acclimatize to the new environment in the myelination medium, ES was provided during the initial stage of myelination (DIV 10). Since ES at frequencies higher than 100 Hz lead to the depression of action potential (AP) of DRG neurons and E-field strengths higher than 50 mV mm^{-1} cause abnormal SC morphology [27], screening was conducted with biphasic ES of 1–100 Hz for 1 h at a field strength of 50 mV mm^{-1}. The efficacy of the ES during the screening was evaluated by the changes in Krox20 expression one day after ES application. Krox20 was chosen because it is a well-known marker for myelinating SCs [28]. It is a master regulator of PNS myelination [29], being vital in both the development as well as maintenance of myelin [30, 31]. In the 1–100 Hz frequency range, 20 Hz ES was the most effective at upregulating Krox20 expression, with almost 2.5-fold upregulation compared to control DRG. On the other hand, 100 Hz ES downregulated Krox20 expression 0.5-fold when compared to control (figure S1(A)). Therefore, biphasic ES was applied at 20 Hz and 50 mV mm^{-1} for 1 h, before carrying out further evaluations with the DRG (figure S1(B)).

A proper time window for evaluating the effects of ES on myelination was determined by monitoring the DRG explant from bright-field images at regular intervals (figure S1(C)). The myelin morphology at the suitable times was further confirmed via confocal imaging. Myelin morphology at 19 DIV was elongated and bipolar (figure S1(D), white arrows), which is characteristic of immature myelin [32]. On the other hand, myelin morphology at 30 DIV was uniform thickness (figure S1(E)), suggesting sufficient progression of myelination [33]. Therefore, the myelination was evaluated via confocal imaging at 19 DIV (figures 3(A) and S2(A)) and 30 DIV (figures 3(B) and S2(B)), which represent the intermediate and mature myelination stages respectively. Upon application of ES, the percentage of neurons containing myelin increased by 129% during the intermediate (figure 3(C)) and 72% during the mature myelination stage (figure 3(E)), compared

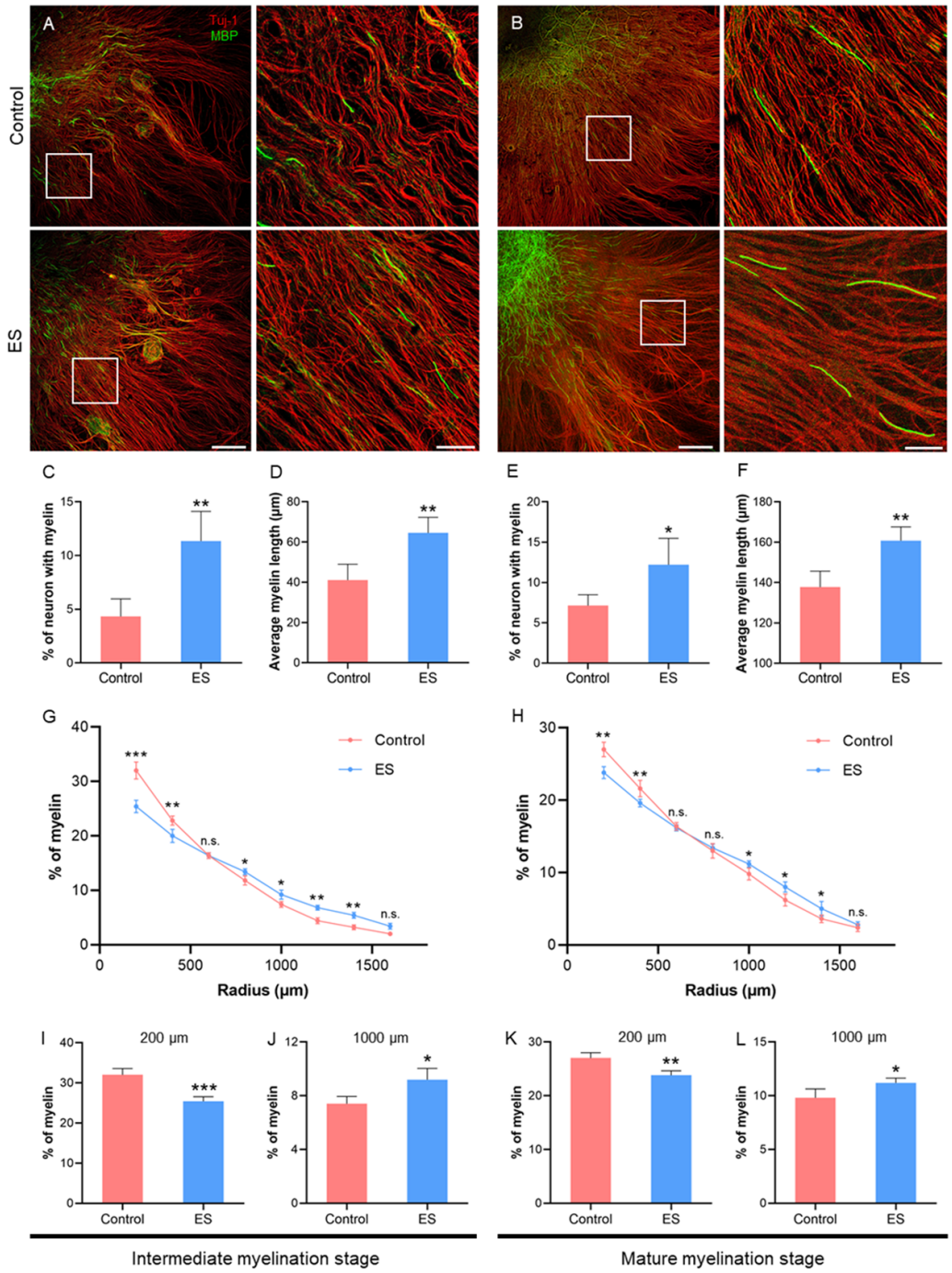

Figure 3. ES enhances myelination in the embryo DRG explant. (A) Representative confocal images of immunostained embryo DRGs during the intermediate myelination stage (Tuj-1, red; MBP, green). The panel on the right shows the enlarged image of the region marked. Scale bar: 500 μm for left-side images and 100 μm for right-side images. (B) Representative confocal images of immunostained embryo DRGs during the mature myelination stage (Tuj-1, red; MBP, green). The panel on the right shows the enlarged image of the region marked. Scale bar: 500 μm for left-side images and 100 μm for right-side images. (C) The percentage of myelinated neurons in the DRG during the intermediate myelination stage ($n = 5$). (D) The average myelin length in the DRG during the intermediate myelination stage ($n = 5$). (E) The percentage of myelinated neurons in the DRG during the mature myelination stage ($n = 5$). (F) The average myelin length in the DRG during the mature myelination stage ($n = 5$). (G) Percentage of myelin in each 200 μm region with increasing proximal-to-distal distance in the DRG during the intermediate myelination stage ($n = 5$). (H) Percentage of myelin in each 200 μm region with increasing proximal-to-distal distance in the DRG during the mature myelination stage ($n = 5$). (I) Percentage of myelin in a region 200 μm from the center of the DRG during the intermediate myelination stage ($n = 5$). (J) Percentage of myelin in a region 1000 μm from the center of the DRG during the intermediate myelination stage ($n = 5$). (K) Percentage of myelin in a region 200 μm from the center of the DRG during the mature myelination stage ($n = 5$). (L) Percentage of myelin in a region 1000 μm from the center of the DRG during the mature myelination stage ($n = 5$). The measurements were taken from five distinct samples for each condition. For the percentage of myelinated neurons ((C) and (E)) and the radial distribution of myelin ((G) and (H)), the entire image was analyzed. For the average length of myelin ((D) and (F)), the lengths of all individual myelin segments in the sample were measured, and then the average length for each sample was recorded. $^{*}p < 0.05$, $^{**}p < 0.005$, $^{***}p < 0.001$. n.s., not significant.

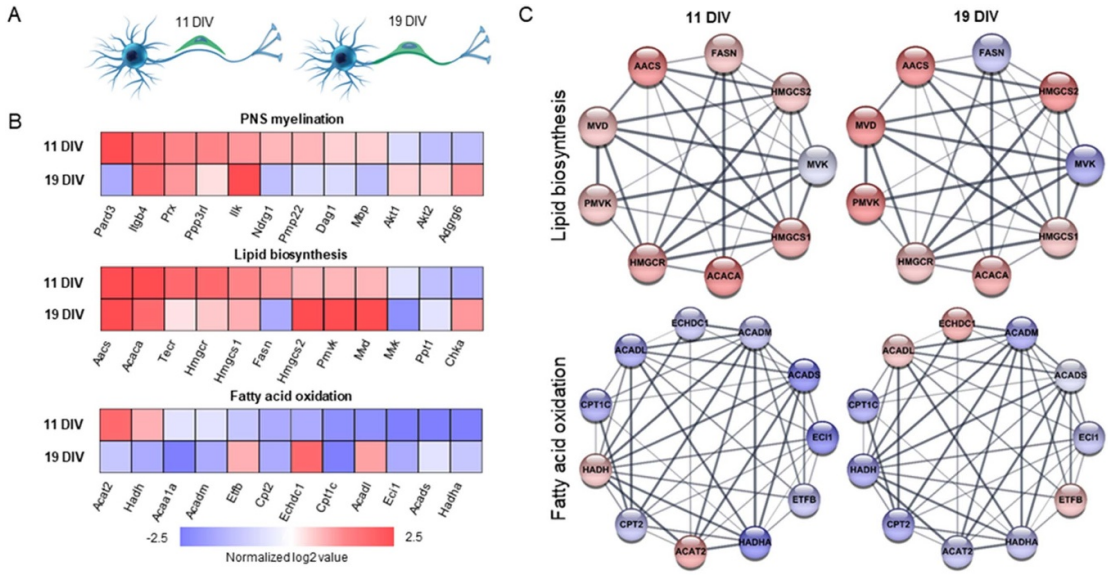

Figure 4. RNA sequencing of the DRG after ES. (A) Schematic showing condition of the DRG myelination at 11 DIV and 19 DIV. At 11 DIV the SC is in alignment with the neuron as it prepares to undergo myelination. At 19 DIV, myelination is underway as the SC extends its cell membrane along the neuron and acquires a bipolar morphology. This is the intermediate stage of myelination. (B) RNA sequencing data showing the relative fold changes in the genes expressed in the embryo DRG after ES compared to the control DRG. The genes were sorted in descending order based on the fold change at 11 DIV. (C) The protein association networks of the genes involved in lipid biosynthesis and fatty acid oxidation, created with STRING. Boldness of the connecting line between two genes represents the strength of the association and the color of the bubble represents the extent of the fold change (red = upregulated, blue = downregulated).

to control DRG. The average length of myelin segments also increased significantly upon ES—61% during the intermediate (figure 3(D)) and 17% during the mature myelination stage (figure 3(F)). Longer myelin segments facilitate neuronal transmission by increasing nerve conduction velocity, as shown in rodents as well as computational models of axons [34, 35]. Although the enhancement of myelination upon ES was comparatively less dramatic at the mature myelination stage, it was still significant, suggesting that ES at the proper time window can have persistently beneficial effects on myelination.

In several demyelinating peripheral neuropathies, the distal region of the axon is relatively more demyelinated than the proximal, making the symptoms such as muscle atrophy and numbness exacerbated in the distal region of the limb [4, 36, 37]. As such, an optimal treatment for these neuropathies should enhance myelination comparatively more in the distal region than in the proximal. Therefore, after verifying that the proposed electroceutical approach enhanced myelination in the whole DRG, its effectiveness for enhancing myelination in the distal region of the DRG was also evaluated. The number of myelin segments was counted in each 200 μm region with increasing radial distance from the center of the DRG. Interestingly, while ES enhanced myelination in both proximal and distal regions, the extent of enhancement was comparatively greater in the distal region (figures S3(A) and (B)). If the extent of myelination enhancement is sufficiently dominant in the distal region, it can alter the distribution of myelin in the DRG. To investigate this, we calculated the percentage of myelin segments in each 200 μm region, based on the total number of myelin segments in the whole DRG. Our results showed that, after ES, the percentage of myelin segments decreased in the proximal region and increased in the distal region (figures 3(G) and (H)), suggesting an alteration in myelin distribution. For example, during the intermediate myelination stage, the percentage of myelin segments decreased by 21% in a proximal region (200 μm) (figure 3(I)) and increased by 24% in a distal region (1000 μm) (figure 3(J)). Likewise, during the mature myelination stage, the percentage of myelin segments decreased by 12% in a proximal region (200 μm) (figure 3(K)) and increased by 14% in a distal region (1000 μm) (figure 3(L)). These results showed that ES effectively enhanced myelination in the distal region of the DRG, which further strengthens its prospect to be an effective intervention for demyelinating peripheral neuropathies.

3.2. ES results in upregulation of lipid biosynthesis in the DRG

Next, the biochemical changes enhancing DRG myelination as a result of ES were evaluated. RNA sequencing was performed on the DRG explants at two different myelination stages—the initial stage at 11 DIV (1 d after ES) and the intermediate stage at 19 DIV (9 d after ES) (figure 4(A)). The gene expressions at these two stages are decisive in the myelination schedule in the DRG [38]. After ES, there is a consistent upregulation of most of the genes involved in PNS

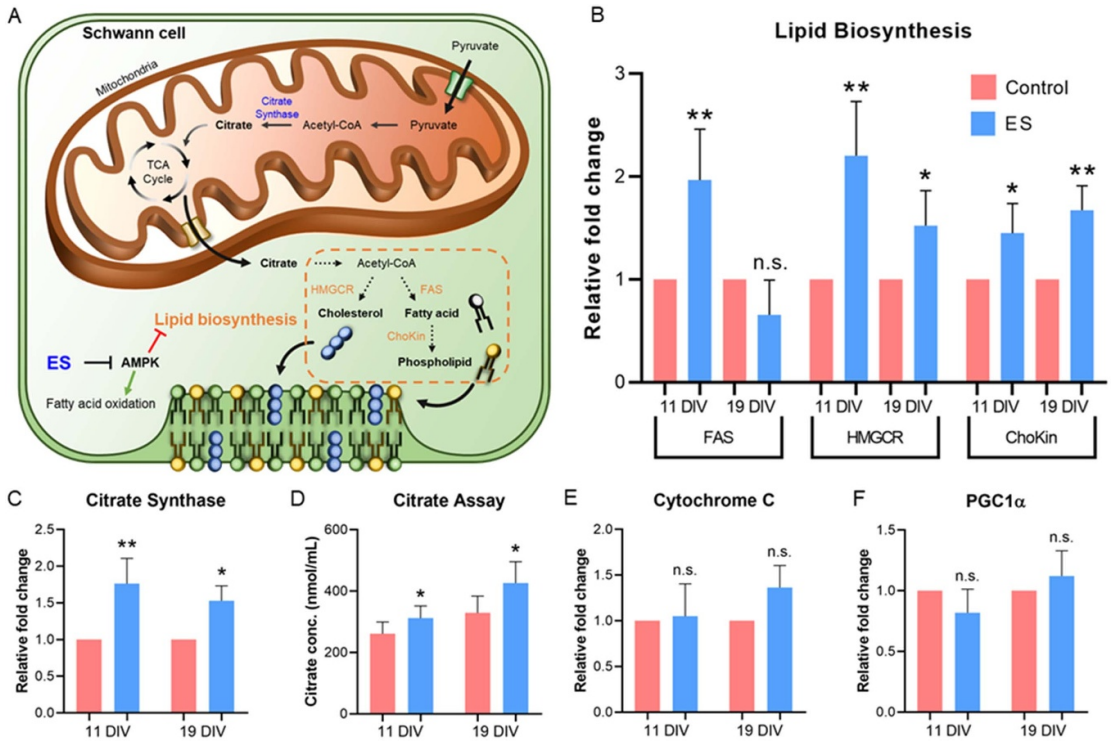

Figure 5. ES upregulates lipid biosynthesis in the DRG. (A) Schematic showing the role of mitochondrial citrate in the lipid biosynthesis process during myelination. The citrate is converted to acetyl-CoA, which is a building block for various myelin membrane lipids. (B) The expression of three representative genes involved in lipid biosynthesis—fatty acid synthase (FAS), HMG-CoA reductase (HMGCR) and choline kinase (ChoKin)—at 11 DIV and 19 DIV ($n = 3$). (C) The expression of citrate synthase at 11 DIV and 19 DIV ($n = 3$). (D) Citrate assay of the embryo DRG to measure available citrate at 11 DIV and 19 DIV ($n = 3$). (E) The expression of cytochrome c at 11 DIV and 19 DIV ($n = 3$). (F) The expression of PGC1α at 11 DIV and 19 DIV ($n = 3$). $^{*}p < 0.05$, $^{**}p < 0.005$. n.s., not significant.

myelination pathway, which conforms to the previous observation from confocal imaging. Interestingly, a similar degree of upregulation as PNS myelination genes was observed in the genes involved in lipid biosynthesis. In both cases, the extent of upregulation is more profound during the initial stage, but is still noticeably persistent during the intermediate stage of myelination. Given that lipid biosynthesis and fatty acid oxidation are connected in reciprocal fashion [39], the genes involved in fatty acid oxidation were also analyzed. At both stages, the RNA sequencing showed a consistent downregulation of the genes involved in the fatty acid oxidation process, where the extent of downregulation was more prominent during the initial stage of the myelination (figure 4(B)). To further support RNA sequencing results, protein association networks of the genes involved in lipid biosynthesis and fatty acid oxidation processes were constructed using STRING. Genes more strongly associated to each other followed consistent regulation patterns—upregulation in the case of lipid biosynthesis and downregulation in fatty acid oxidation—further strengthening the outcome of RNA sequencing (figure 4(C)). Therefore, this suggests a novel finding that the ES increases lipid biosynthesis in the DRG, leading to enhancement in myelination.

This increase in PNS lipid biosynthesis upon ES might be due to its close association with myelination. The myelin membrane is exceptionally rich in lipids [40]. As such, SCs undergo a demanding lipid biosynthesis regime during the assembly of myelin. The impairment of this *de novo* lipid synthesis regime might cause hypomyelination [41]. Furthermore, lipid supplementation is effective at rescuing the demyelinating phenotype in animal models of CMT [7, 8, 42]. The lipid biosynthesis in SCs is intertwined with mitochondrial metabolism. During the citric acid cycle, the mitochondria produce citrate, which can then have two possible fates: (a) it can continue along the citric acid cycle, where it will be used for the purpose of energetics, or (b) it can move into the cytosol and then be converted to acetyl-CoA, a molecule necessary for *de novo* fatty acid synthesis by SCs [43]. These fatty acids serve as building blocks for most of the structural lipids of myelin [40, 44]. Therefore, defects in SC mitochondria can cause significant loss of myelin [45, 46]. Given how indispensable lipid biosynthesis is during myelination and how closely it is associated with mitochondrial citrate (figure 5(A)), further analyses via qPCR and biochemical assays were performed to investigate the shift towards increased lipid biosynthesis.

Since FAS, HMGCR and ChoKin are critically involved in the synthesis of three key components, fatty acids, cholesterol and phospholipids, respectively, expressions of the three representative genes were compared. In accordance with the RNA sequencing data, the qPCR also revealed a significant upregulation of the lipid biosynthesis genes after ES. At 11 DIV, there was a 1.9-fold increase in FAS expression, a 2.2-fold increase in HMGCR expression and a 1.4-fold increase in the ChoKin expression, when compared to the control DRG (figure 5(B)). To verify whether mitochondrial citrate is being utilized to achieve higher lipid biosynthesis, the gene expression of citrate synthase in the DRG explant was measured. ES significantly increased the citrate synthase expression compared to control in the DRG explant, at both stages (figure 5(C)). This was further validated via citrate assay in the DRG explant. Compared to control, the available citrate concentration after ES was 20% higher at 11 DIV and 30% higher at 19 DIV (figure 5(D)). In order to verify that the additional citrate from the mitochondria is being utilized for lipid biosynthesis and not for energetics, we analyzed the expression of two representative genes responsible for mitochondrial energetics: cytochrome c and PGC1α. Our results showed that, after ES, there were no significant changes in the expressions of cytochrome c and PGC1α at either stage of myelination (figures 5(E) and (F)). These results suggest that, as a consequence of ES application, mitochondrial citrate is utilized to support higher lipid biosynthesis, further used to construct myelin.

For further verification, the changes in fatty acid oxidation were also analyzed. Lipid biosynthesis and fatty acid oxidation are regulated via AMP-activated protein kinase (AMPK) signaling, and an elevated level of AMPK reduces lipid biosynthesis, which hinders the myelination process [39]. Interestingly, AMPK expression decreased significantly at both time points after ES (figure S4(A)). Additionally, 3-hydroxyacyl-CoA dehydrogenase (HADH)—which is a representative enzyme in fatty acid oxidation—also shows a significant downregulation at both 11 DIV and 19 DIV upon ES, compared to control DRG (figure S4(B)). Carnitine is required for the transport of fatty acids into the mitochondrial matrix during fatty acid oxidation [47]. Since carnitine assay is well-regarded as a measure of fatty acid oxidation, it was conducted at both 11 DIV and 19 DIV to further support the outcome revealed by qPCR. After ES, carnitine concentration is reduced by 39% at 11 DIV and 44% at 19 DIV compared to control DRG (figure S4(C)). The downregulated expressions of AMPK and HADH and the reduced carnitine concentration confirm that there is a net shift towards higher lipid biosynthesis in the DRG after ES, resulting from the upregulation in lipid biosynthesis and downregulation in fatty acid oxidation.

3.3. ES increases cholesterol and sphingomyelin abundance in the DRG myelin membrane

In order to validate whether the upregulation in lipid biosynthesis makes higher abundance of structural lipids in the myelin membrane, ToF-SIMS imaging was performed. ToF-SIMS is an analytical technique to study surface distribution of target chemical species. Due to shallow sampling depth and recently developed implementations in *in vitro* sample preparation techniques for ToF-SIMS, it is suitable for imaging surface lipids with minimal interference from intracellular lipids [48–51]. To the best of our knowledge, this is the first reported analysis of myelin lipids in DRG explants via ToF-SIMS imaging. Due to the relatively higher density of cholesterol and sphingomyelin in the myelin membrane [40], these two structural lipids were of primary importance during positive-mode ToF-SIMS. Compared to the control DRG, ES resulted in noticeably higher abundance of cholesterol and sphingomyelin in the DRG myelin. Particularly, ToF-SIMS images of the cholesterol fragment showed clear myelin-like segments along radial patterns in the DRG explant. Such fragments were more prominent in the ES DRG (figure 6(A), green arrows) compared to the control (figure 6(A), sky-blue arrows). We then analyzed the size distribution of the cholesterol and sphingomyelin-enriched fragments. ES led to a significantly lower frequency of fragments in the smallest size group and a significantly higher frequency of fragments in the medium size groups in case of both cholesterol (figure 6(B)) and sphingomyelin (figure 6(C)). Meanwhile, in both cases, the frequency of fragments in the largest size group did not show any significant change.

After the membrane layer was sufficiently eroded, ToF-SIMS was carried out in negative mode to analyze intracellular fatty acids such as palmitic, oleic and stearic acids. As the fatty acids are free molecules within the cytosol, the myelin-like segments were not observed. However, in accordance with the qPCR data, there is a noticeable increase in concentrations of fatty acids distributed across the DRG (figure S5). These ToF-SIMS images further validate that ES leads to an increase in lipid biosynthesis, eventually resulting in increase in structural lipids that make up myelin.

4. Discussion

Here, we demonstrated the enhancement of myelination in the DRG explant via ES, resulting from upregulation in lipid biosynthesis and better structural lipid abundance in the myelin membrane. We confirmed the results from immunocytochemistry, RNA sequencing, qPCR and chemical assays at sequential stages of the myelination process, followed by the analysis of myelin lipids via ToF-SIMS. Recently, electroceuticals have emerged as effective treatments for

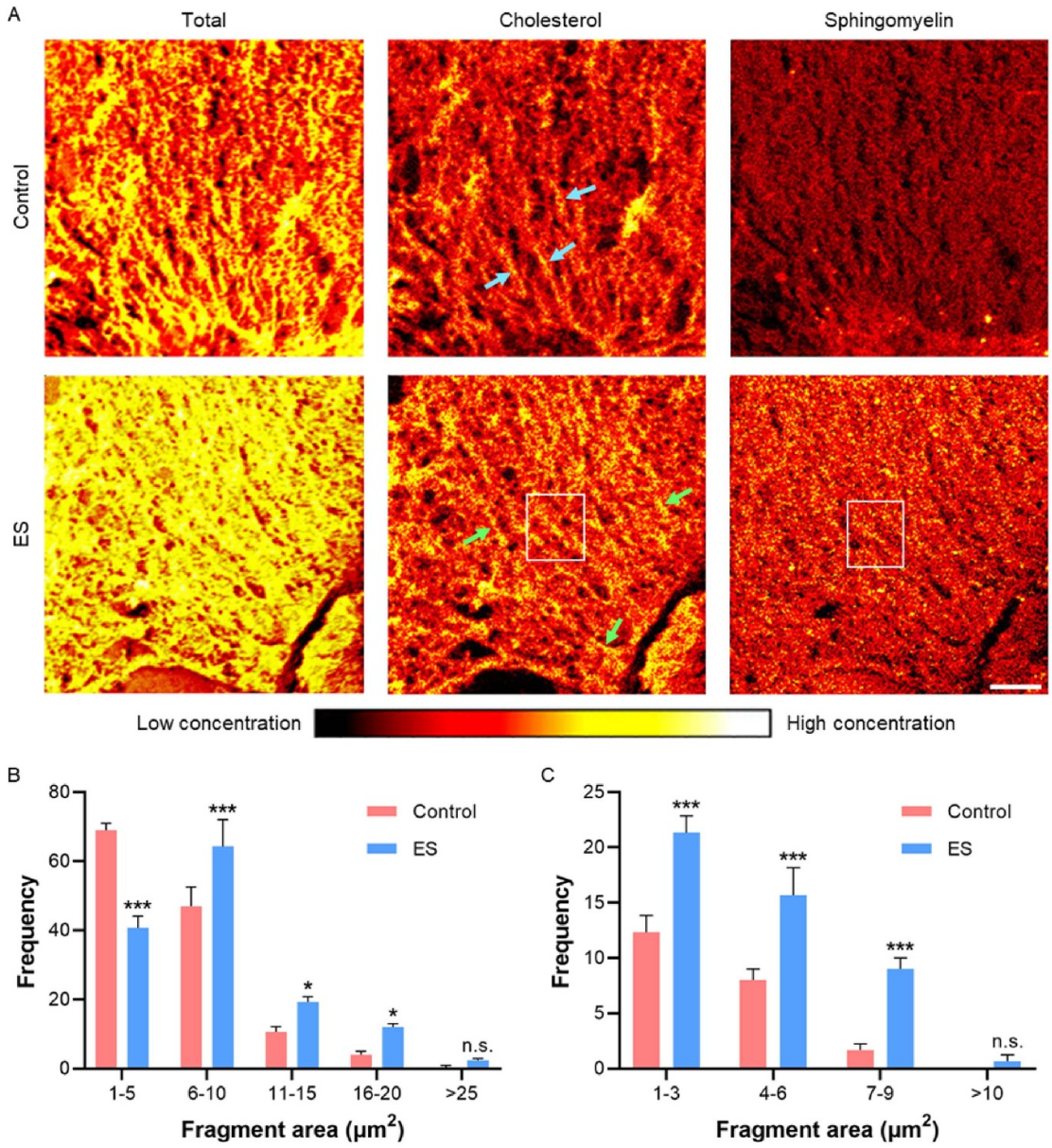

Figure 6. ES increases cholesterol and sphingomyelin abundance in the DRG myelin membrane. (A) ToF-SIMS images of DRG at 30 DIV taken using positive mode. Arrows point to representative cholesterol-rich fragments. Scale bar: 100 μm. (B) Frequency of cholesterol-rich fragments of different size groups. (C) Frequency of sphingomyelin-rich fragments of different size groups. $^{*}p < 0.05$, $^{**}p < 0.005$, $^{***}p < 0.001$. n.s., not significant.

central nervous system (CNS) neuropathies, such as Parkinson's disease, epilepsy, paraplegia, obsessive-compulsive disorder and spinal cord injury [52–54]. Compared to the CNS, however, the effectiveness of electroceutical interventions for neuropathies of the PNS are less actively studied. In particular, the myelination-enhancing effects of electroceuticals in the PNS had rarely been investigated.

For our study, we utilized the mouse DRG explant as an *ex vivo* model of the PNS [22]. We have evaluated the effects of electroceuticals at two distinct stages of the myelination process. SCs have remarkable neuroplasticity that allows persistent myelin repair over a long time period. Our results suggest that the ES application has long-lasting benefits towards enhancing myelination in the DRG explant. Another interesting finding was that ES enhanced myelination in the distal region of the DRG neurons. A plausible reason for this could be the ability of ES to mimic the effect of the AP of neurons [55]. The AP along the axon can be detected by the adjacent SCs, which triggers a pro-myelinating response in the SCs [56]. Since the AP gets weaker as it propagates along the axon, its pro-myelinating effect diminishes in the distal region of the neuron. We postulate that, the ES mimicked the effect of the AP on the SCs, which reinforced the pro-myelinating response in the distal region of the neuron.

Our findings regarding the enhancement of DRG myelination upon ES were further supported by the gene expression analysis using RNA sequencing, which showed that myelination-related genes were

consistently upregulated after ES. The only exception was the expression of MBP. Although the confocal images showed higher MBP levels in the DRG at 19 DIV upon ES application, the RNA sequencing data showed a slight downregulation at 19 DIV. This is likely because SCs tend to express slightly lower mRNA levels of MBP as they mature, while the protein level of MBP tends to increase [28]. In this study, we have performed RNA sequencing on the whole DRG, since it has a high suitability towards understanding the effectiveness of ES for enhancing PNS myelination. In future studies, performing RNA sequencing on neurons and SCs separately would offer further understanding towards the changes in gene expression after ES.

The deficiency in lipid biosynthesis is responsible for several demyelinating PNS neuropathies [6]. While ES application enhanced the *de novo* lipid biosynthesis, this effect was more considerable during the initial stage of myelination. This is probably because the SCs synthesize myelin membrane at a faster rate during the initial stage, thus putting a greater emphasis on the lipid biosynthesis during this stage [29, 57]. The ES-mediated upregulation in lipid biosynthesis can potentially avoid the systemic side effects of exogenous lipid supplementation that has been proposed for treatment of demyelinating CMT, the most prevalent inherited neuropathy worldwide. ES also led to higher abundance of cholesterol and sphingomyelin in the myelin membrane. These structural lipids are vital during the assembly of myelin and also provide myelin membrane stability by anchoring to myelin proteins in lipid-rich regions of the membrane called lipid rafts [58–61], which play a crucial role in myelin compaction as well as regulation of promyelinating pathways [62, 63]. Therefore, an electroceutical approach can potentially lead to structurally and functionally better myelin membranes in demyelinating PNS neuropathies.

To optimize our approach, a few modifications can be considered. First, multiple sessions of ES at regular intervals during the myelination process can be applied, to evaluate if this can enhance the myelination even further. Second, the frequency-dependent effect of ES on myelination could be investigated further. It should be noted that low-frequency ES has already been shown to be beneficial for PNS application, such as promoting axonal regeneration after injury and neurotrophic factor release [16, 17, 19]. Meanwhile, high-frequency ES can exhaust the propagation of axonal AP, which is used to block the unwanted nerve conduction that occurs during neuropathic pain and spasticity [64]. In order for electroceuticals to translate towards application in human patients, there needs to be further maturation of the implantable neural interfaces [65]. Recently, there has been intensive research on soft, biocompatible and electro-active materials that can minimize the foreign body reaction and the physical mismatch at the nerve-electrode boundary, making them more suitable for long-term implantation [66]. Additionally, the recent developments in miniature, wireless and battery-free implantable neural interfaces have made electroceuticals considerably less invasive [67]. Our results are potentially a starting platform for the wider application of electroceuticals for demyelinating peripheral neuropathies. With further elucidation of the mechanistic changes and advancement in implantable neural interfaces, we expect that electroceuticals will reach clinical translation to treat human patients suffering from such neuropathies.

5. Conclusion

The loss of myelin in the PNS leads to peripheral demyelinating diseases, most of which currently have no available treatment. Here, we demonstrated that an electroceutical approach can enhance myelination in the mouse DRG, a representative *ex vivo* model of the PNS. After ES, the percentage of myelinated neurons and the average myelin length in the DRG were significantly enhanced. Further analysis showed that ES induced lipid biosynthesis in the DRG and increased the abundance of the structural lipids in the myelin membrane. Due to the association of the deficiency in lipid biosynthesis with several peripheral demyelinating diseases, this work lays the groundwork for future electroceutical-based treatment for such neuropathies.

Data availability statement

All data that support the findings of this study are included within the article (and any supplementary files).

Acknowledgments

We acknowledge Dr Hanwoong Woo for his valuable suggestions. This research was supported by the Samsung Research Funding and Incubation Center for Future Technology (SRFC) (Grant No. SRFC-IT1701-10).

Conflict of interest

The authors declare no competing interests.

ORCID iDs

Aseer Intisar https://orcid.org/0000-0001-9946-3707
Woon-Hae Kim https://orcid.org/0000-0002-1536-5374
Minseok S Kim https://orcid.org/0000-0002-4268-6886

References

[1] Stadelmann C, Timmler S, Barrantes-Freer A and Simons M 2019 Myelin in the central nervous system: structure, function, and pathology *Physiol. Rev.* **99** 1381–431

[2] Suter U, Moskow J J, Welcher A A, Snipes G J, Kosaras B, Sidman R L, Buchberg A M and Shooter E M 1992 A leucine-to-proline mutation in the putative first transmembrane domain of the 22 kDa peripheral myelin protein in the trembler-J mouse *Proc. Natl Acad. Sci. USA* **89** 4382–6

[3] Jessen K R and Mirsky R 2016 The repair Schwann cell and its function in regenerating nerves *J. Physiol.* **594** 3521–31

[4] Kamil K, Yazid M D, Idrus R B H, Das S and Kumar J 2019 Peripheral demyelinating diseases: from biology to translational medicine *Front. Neurol.* **10** 87

[5] Barreto L C L S, Oliveira F S, Nunes P S, de Franca Costa I M P, Garcez C A, Goes G M, Neves E L A, de Souza Siqueira Quintans J and de Souza Araujo A A 2016 Epidemiologic study of Charcot-Marie-Tooth disease: a systematic review *Neuroepidemiology* **46** 157–65

[6] Verheijen M H G, Chrast R, Burrola P and Lemke G 2003 Local regulation of fat metabolism in peripheral nerves *Genes Dev.* **17** 2450–64

[7] Fledrich R *et al* 2018 Targeting myelin lipid metabolism as a potential therapeutic strategy in a model of CMT1A neuropathy *Nat. Commun.* **9** 3025

[8] Zhou Y, Bazick H, Miles J R, Fethiere A I, Salihi M O A, Fazio S, Tavori H and Notterpek L 2019 A neutral lipid-enriched diet improves myelination and alleviates peripheral nerve pathology in neuropathic mice *Exp. Neurol.* **321** 113031

[9] Wang Z *et al* 2011 Gut flora metabolism of phosphatidylcholine promotes cardiovascular disease *Nature* **472** 57–63

[10] Tang W H, Wang Z, Levison B S, Koeth R A, Britt E B, Fu X, Wu Y and Hazen S L 2013 Intestinal microbial metabolism of phosphatidylcholine and cardiovascular risk *New Engl. J. Med.* **368** 1575–84

[11] Lackey D E, Lazaro R G, Li P, Johnson A, Hernandez-Carretero A, Weber N, Vorobyova I, Tsukomoto H and Osborn O 2016 The role of dietary fat in obesity-induced insulin resistance *Am. J. Physiol. Endocrinol. Metab.* **311** E989–97

[12] Huypens P, Sass S, Wu M, Dyckhoff D, Tschop M, Theis F, Marschall S, Hrabe de Angelis M and Beckers J 2016 Epigenetic germline inheritance of diet-induced obesity and insulin resistance *Nat. Genet.* **48** 497–9

[13] Passage E, Norreel J C, Noack-Fraissignes P, Sanguedolce V, Pizant J, Thirion X, Robaglia-Schlupp A, Pellissier J F and Fontes M 2004 Ascorbic acid treatment corrects the phenotype of a mouse model of Charcot-Marie-Tooth disease *Nat. Med.* **10** 396–401

[14] Pareyson D *et al* 2011 Ascorbic acid in Charcot-Marie-Tooth disease type 1A (CMT-TRIAAL and CMT-TRAUK): a double-blind randomised trial *Lancet Neurol.* **10** 320–8

[15] Mathis S, Magy L and Vallat J-M 2015 Therapeutic options in Charcot-Marie-Tooth diseases *Expert Rev. Neurother.* **15** 355–66

[16] Al-Majed A A, Neumann C M, Brushart T M and Gordon T 2000 Brief electrical stimulation promotes the speed and accuracy of motor axonal regeneration *J. Neurosci.* **20** 2602–8

[17] Geremia N M, Gordon T, Brushart T M, Al-Majed A A and Verge V M K 2007 Electrical stimulation promotes sensory neuron regeneration and growth-associated gene expression *Exp. Neurol.* **205** 347–59

[18] Kim I S, Song Y M, Cho T H, Pan H, Lee T H, Kim S J and Hwang S J 2011 Biphasic electrical targeting plays a significant role in Schwann cell activation *Tissue Eng.* A **17** 1327–40

[19] Huang J, Ye Z, Hu X, Lu L and Luo Z 2010 Electrical stimulation induces calcium-dependent release of NGF from cultured Schwann cells *Glia* **58** 622–31

[20] Kumar P J, Adams R D, Harkins A B, Engeberg E D and Willits R K 2016 Stimulation frequency alters the dorsal root ganglion neurite growth and directionality *in vitro IEEE Trans. Biomed. Eng.* **63** 1257–68

[21] Vuka I, Vucic K, Repic T, Ferhatovic Hamzic L, Sapunar D and Puljak L 2018 Electrical stimulation of dorsal root ganglion in the context of pain: a systematic review of *in vitro* and *in vivo* animal model studies *Neuromodulation* **21** 213–24

[22] Monje P V 2020 Schwann cell cultures: biology, technology and therapeutics *Cells* **9** 1848–71

[23] Koopmeiners A S, Mueller S, Kramer J and Hogan Q H 2013 Effect of electrical field stimulation on dorsal root ganglion neuronal function *Neuromodulation* **16** 304–11

[24] Langmead B and Salzberg S L 2012 Fast gapped-read alignment with Bowtie 2 *Nat. Methods* **9** 357–9

[25] Quinlan A R and Hall I M 2010 BEDTools: a flexible suite of utilities for comparing genomic features *Bioinformatics* **26** 841–2

[26] Robinson M D, McCarthy D J and Smyth G K 2010 edgeR: a bioconductor package for differential expression analysis of digital gene expression data *Bioinformatics* **26** 139–40

[27] Koppes A N, Nordberg A L, Paolillo G M, Goodsell N M, Darwish H A, Zhang L and Thompson D M 2014 Electrical stimulation of Schwann cells promotes sustained increases in neurite outgrowth *Tissue Eng.* A **20** 494–506

[28] Liu Z, Jin Y-Q, Chen L, Wang Y, Yang X, Cheng J, Wu W, Qi Z, Shen Z and Vinci M C 2015 Specific marker expression and cell state of Schwann cells during culture *in vitro PLoS One* **10** e0123278

[29] Salzer J L 2015 Schwann cell myelination *Cold Spring Harb. Perspect. Biol.* **7** a020529

[30] Topilko P, Schneider-Maunoury S, Levi G, Baron-van evercooren A B-V, Chennoufi A B Y, Seitanidou T, Babinet C and Charnay P 1994 Krox20 controls myelination in the peripheral nervous system *Nature* **371** 796–9

[31] Decker L, Desmarquet-Trin-Dinh C, Taillebourg E, Ghislain J, Vallat J M and Charnay P 2006 Peripheral myelin maintenance is a dynamic process requiring constant Krox20 expression *J. Neurosci.* **26** 9771–9

[32] Tricaud N 2017 Myelinating Schwann cell polarity and mechanically-driven myelin sheath elongation *Front. Cell. Neurosci.* **11** 414

[33] Hyung S, Yoon Lee B, Park J-C, Kim J, Hur E-M and Francis Suh J-K 2015 Coculture of primary motor neurons and Schwann cells as a model for *in vitro* myelination *Sci. Rep.* **5** 15122

[34] Arancibia-Carcamo I L, Ford M C, Cossell L, Ishida K, Tohyama K and Attwell D 2017 Node of Ranvier length as a potential regulator of myelinated axon conduction speed *eLife* **6** e23329–43

[35] Walsh D M, Landman K A and Hughes B D 2017 What is the optimal distribution of myelin along a single axon? *Neurosci. Lett.* **658** 97–101

[36] Kim H S, Yoon Y C, Choi B-O, Jin W and Cha J G 2019 Muscle fat quantification using magnetic resonance imaging: case-control study of Charcot-Marie-Tooth disease patients and volunteers *J. Cachexia Sarcopenia Muscle* **10** 574–85

[37] Hattori N *et al* The Study Group for Hereditary Neuropathy in Japan 2003 Demyelinating and axonal features of Charcot-Marie-Tooth disease with mutations of myelin-related proteins (PMP22, MPZ and Cx32): a clinicopathological study of 205 Japanese patients *Brain* **126** 134–51

[38] Kangas S M, Ohlmeier S, Sormunen R, Jouhilahti E-M, Peltonen S, Peltonen J and Heape A M 2016 An approach to comprehensive genome and proteome expression analyses in Schwann cells and neurons during peripheral nerve myelin formation *J. Neurochem.* **138** 830–44

[39] Beirowski B 2019 The LKB1-AMPK and mTORC1 metabolic signaling networks in Schwann cells control axon integrity and myelination *Bioessays* **41** e1800075

[40] Chrast R, Saher G, Nave K-A and Verheijen M H G 2011 Lipid metabolism in myelinating glial cells: lessons from human inherited disorders and mouse models *J. Lipid Res.* **52** 419–34
[41] Montani L *et al* 2018 De novo fatty acid synthesis by Schwann cells is essential for peripheral nervous system myelination *J. Cell Biol.* **217** 1353–68
[42] Sahenk Z, Yalvac M E, Amornvit J, Arnold W D, Chen L, Shontz K M and Lewis S 2018 Efficacy of exogenous pyruvate in trembler^{J} mouse model of Charcot-Marie-Tooth neuropathy *Brain Behav.* **8** e01118
[43] Ino D and Iino M 2017 Schwann cell mitochondria as key regulators in the development and maintenance of peripheral nerve axons *Cell. Mol. Life Sci.* **74** 827–35
[44] Poitelon Y, Kopec A M and Belin S 2020 Myelin fat facts: an overview of lipids and fatty acid metabolism *Cells* **9** 812–28
[45] Beirowski B, Babetto E, Golden J P, Chen Y-J, Yang K, Gross R W, Patti G J and Milbrandt J 2014 Metabolic regulator LKB1 is crucial for Schwann cell-mediated axon maintenance *Nat. Neurosci.* **17** 1351–61
[46] Viader A, Sasaki Y, Kim S, Strickland A, Workman C S, Yang K, Gross R W and Milbrandt J 2013 Aberrant Schwann cell lipid metabolism linked to mitochondrial deficits leads to axon degeneration and neuropathy *Neuron* **77** 886–98
[47] Longo N, Frigeni M and Pasquali M 2016 Carnitine transport and fatty acid oxidation *Biochim. Biophys. Acta* **1863** 2422–35
[48] Kraft M L and Klitzing H A 2014 Imaging lipids with secondary ion mass spectrometry *Biochim. Biophys. Acta* **1841** 1108–19
[49] Lim H, Lee S Y, Park Y, Jin H, Seo D, Jang Y H and Moon D W 2021 Mass spectrometry imaging of untreated wet cell membranes in solution using single-layer graphene *Nat. Methods* **18** 316–20
[50] Lim H, Lee S Y, Moon D W and Kim J Y 2019 Preparation of cellular samples using graphene cover and air-plasma treatment for time-of-flight secondary ion mass spectrometry imaging *RSC Adv.* **9** 28432–8
[51] Lee S Y, Lim H, Moon D W and Kim J Y 2019 Improved ion imaging of slowly dried neurons and skin cells by graphene cover in time-of-flight secondary ion mass spectrometry *Biointerphases* **14** 051001
[52] Famm K, Litt B, Tracey K J, Boyden E S and Slaoui M 2013 A jump-start for electroceuticals *Nature* **496** 159–61
[53] Courtine G and Sofroniew M V 2019 Spinal cord repair: advances in biology and technology *Nat. Med.* **25** 898–908
[54] Grover S, Nguyen J A, Viswanathan V and Reinhart R M G 2021 High-frequency neuromodulation improves obsessive-compulsive behavior *Nat. Med.* **27** 232–8
[55] Radivojevic M, Jackel D, Altermatt M, Muller J, Viswam V, Hierlemann A and Bakkum D J 2016 Electrical identification and selective microstimulation of neuronal compartments based on features of extracellular action potentials *Sci. Rep.* **6** 31332
[56] Samara C, Poirot O, Domenech-Estevez E and Chrast R 2013 Neuronal activity in the hub of extrasynaptic Schwann cell-axon interactions *Front. Cell. Neurosci.* **7** 1–11
[57] Sherman D L and Brophy P J 2005 Mechanisms of axon ensheathment and myelin growth *Nat. Rev. Neurosci.* **6** 683–90
[58] Lee S, Amici S, Tavori H, Zeng W M, Freeland S, Fazio S and Notterpek L 2014 PMP22 is critical for actin-mediated cellular functions and for establishing lipid rafts *J. Neurosci.* **34** 16140–52
[59] Vinson M *et al* 2003 Lipid rafts mediate the interaction between myelin-associated glycoprotein (MAG) on myelin and MAG-receptors on neurons *Mol. Cell. Neurosci.* **22** 344–52
[60] Fasano A, Amoresano A, Rossano R, Carlone G, Carpentieri A, Liuzzi G M, Pucci P and Riccio P 2008 The different forms of PNS myelin P0 protein within and outside lipid rafts *J. Neurochem.* **107** 291–301
[61] Marinko J T, Kenworthy A K and Sanders C R 2020 Peripheral myelin protein 22 preferentially partitions into ordered phase membrane domains *Proc. Natl Acad. Sci. USA* **117** 14168–77
[62] Aureli M, Grassi S, Prioni S, Sonnino S and Prinetti A 2015 Lipid membrane domains in the brain *Biochim. Biophys. Acta* **1851** 1006–16
[63] Lee D W, Banquy X, Kristiansen K, Kaufman Y, Boggs J M and Israelachvili J N 2014 Lipid domains control myelin basic protein adsorption and membrane interactions between model myelin lipid bilayers *Proc. Natl Acad. Sci. USA* **111** E768–75
[64] Avendano-Coy J, Serrano-Munoz D, Taylor J, Goicoechea-Garcia C and Gomez-Soriano J 2018 Peripheral nerve conduction block by high-frequency alternating currents: a systematic review *IEEE Trans. Neural Syst. Rehabil. Eng.* **26** 1131–40
[65] Birmingham K, Gradinaru V, Anikeeva P, Grill W M, Pikov V, McLaughlin B, Pasricha P, Weber D, Ludwig K and Famm K 2014 Bioelectronic medicines: a research roadmap *Nat. Rev. Drug Discov.* **13** 399–400
[66] Lacour S P, Courtine G and Guck J 2016 Materials and technologies for soft implantable neuroprostheses *Nat. Rev. Mater.* **1** 1–14
[67] Won S M, Cai L, Gutruf P and Rogers J A 2021 Wireless and battery-free technologies for neuroengineering *Nat. Biomed. Eng.* (https://doi.org/10.1038/s41551-021-00683-3)